Effects of pore widening vs oxygenation on capacitance of activated Carbon in aqueous sodium sulfate electrolyte

Lixing Zhang, Yuqin Chi, Zhen Li, Xiaolei Sun, Huazhi Gu, Haijun Zhang, Yao Chen and George Zheng Chen

University of Nottingham Ningbo China, 199 Taikang East Road, Ningbo, 315100, Zhejiang, China.

First published 2020

University of Nottingham
UK | CHINA | MALAYSIA

Effects of pore widening versus oxygenation on capacitance of activated carbon in aqueous sodium sulfate electrolyte

Lixing Zhang,[1] Yuqin Chi,[1] Xiaolei Sun,[5] Huazhi Gu,[1] Haijun Zhang,[1] Zhen Li,[2] Yao Chen,[1,z] and George Zheng Chen[1,3,4]

[1] The State Key Laboratory of Refractories and Metallurgy, College of Materials and Metallurgy, Wuhan University of Science and Technology, Wuhan 430081, China.

[2] Engineering Research Center of Nano-Geo Materials of Ministry of Education, China University of Geosciences, Wuhan 430074, China

[3] Department of Chemical and Environmental Engineering, Faculty of Engineering, University of Nottingham, Nottingham NG2 7RD, UK.

[4] Department of Chemical and Environmental Engineering, Faculty of Science and Engineering, University of Nottingham Ningbo China, Ningbo 315100, China.

[5] School of Materials Science and Engineering & National Institute for Advanced Materials, Tianjin Key Lab for Rare Earth Materials and Applications, Centre for Rare Earth and Inorganic Functional Materials, Nankai University, Tianjin 300350, China

[z] Corresponding author. E-mail: y.chen@wust.edu.cn

Abstract

The commercial activated carbon has a relatively low specific capacitance in the Na_2SO_4 electrolyte, which hinder the development of asymmetrical supercapacitors with high voltage. Re-activation and oxidative etching methods were applied to change the pore structure of activated carbon, respectively, to study the capacitive behavior of carbon in the Na_2SO_4 electrolyte. The pore distributions combining with capacitive properties deduce that 0.85 nm is the threshold diameter of the ion-accessible micropores for hydrated Na^+ and SO_4^{2-}. The specific capacitances of both the carbon materials by re-activation and oxidative etching methods are increased by 40 %, in comparison with the commercial activated carbon. The enhanced capacitive performances of the carbon materials were mainly attributed to the increased ion-accessible specific surface area and pseudocapacitance, respectively. The oxidative etching is a more facile and economical method for practice application. Combining with MnO_2 as the positive electrode, the asymmetrical supercapacitor with a high voltage of 1.8 V exhibits a maximum specific cell capacitance of 50 F g^{-1} and specific energy of 22.5 Wh kg^{-1}.

Keywords: activated carbon; re-activation; oxidative etching; sodium sulfate; asymmetrical supercapacitor

Introduction

Supercapacitors, one of energy storage devices, possess higher energy density than conventional electrostatic capacitors and higher power density than secondary batteries. They can be used to complement or replace secondary batteries in the energy storage field, such as smart grid, electric vehicles, load cranes and emergency doors.[1-3] Activated carbons which are based on electrical double layer (EDL) mechanism without faradic reaction have the unique advantages of long lifetime, high power density and low cost.[4-6] Nowadays, they have been widely employed as commercial electrode materials for supercapacitors.[7-9]

The main efforts in current research on supercapacitors focus on increasing their specific energy, which is proportional to the specific capacitance and the square of the working voltage. The working voltage is mainly associated with the property of electrolyte.[10,11] Although organic electrolytes have higher achievable voltages, aqueous electrolytes have higher electrical conductivity, better safety and environmental benignity and lower cost. The conventional aqueous electrolytes for AC are H_2SO_4 and KOH solution, which have only 1 V cell voltage. Recently, much less corrosive neutral Na_2SO_4 began to be used as the aqueous electrolyte for symmetrical or asymmetrical supercapacitors, the potential window of which reaches 1.6–2 V.[12-14] The great extension of the potential window in Na_2SO_4 electrolyte makes it possible to increase specific energy of aqueous supercapacitors.[15] However, the same commercial AC generally has a much lower specific capacitance in the neutral Na_2SO_4 electrolyte than in those acidic or alkaline ones.[16, 17] So far, the relationship between the pores of carbon

and solvated ions of organic electrolytes has been studied,[18] which asserted that the ions with highly distorted solvated shell could be squeezed into the pores. However, similar studies in the aqueous Na_2SO_4 electrolyte was rarely reported.[19] Therefore, it is essential to fully understand the capacitive behavior of carbon electrodes in order to improve their specific capacitances in Na_2SO_4 based electrolytes.

In this work, we employed two methods to change the pore structure of a commercial activated carbon (AC, YP50f, Kuraray Group) by re-activation and oxidative etching with $Zn(NO_3)_2$ and $KMnO_4$, which were denoted as Zn-AC and Mn-AC, respectively. Both modified samples possessed specific capacitances of 132 F g^{-1}, which were higher than 94 F g^{-1} for the commercial AC at 1 A g^{-1} in Na_2SO_4. However, the pore distributions of Zn-AC and Mn-AC were different. The relationship between pore and ions of Na_2SO_4 was discussed through the specific capacitance. As we know, re-activation with $Zn(NO_3)_2$ needs annealing at high temperature above 500 °C. Therefore, oxidative etching with $KMnO_4$ at room temperature is much more facile and economic approach to improve the specific capacitance of carbon for practical application.[20] Based on the Mn-AC and MnO_2, the asymmetrical supercapacitors in the Na_2SO_4 electrolyte exhibited 22.5 Wh kg^{-1} of specific energy at 0.5 A g^{-1}.

2. Experimental

2.1 Preparation of samples

Re-activation. 1 g AC and 3.6 g $Zn(NO_3)_2$ were dissolved in 10 mL water and sonicated for 15 min and aged for 18 h. The extra $Zn(NO_3)_2$ was removed by vacuum

filtration, then the left solid was dried at 90 °C for 3 h and annealed at 500 °C for 1 h in Ar. The product was dispersed into 1 ml hydrochloric acid in 100 ml water and subsequently stirred for 30 min. Finally, the Zn-AC sample was obtained by centrifugation, washing and desiccation.

Oxidative etching. 0.08 g AC and 0.164 g $KMnO_4$ were dissolved in 27 mL water and then aged for 5 days. The resulted deposit was treated with HCl/H_2O_2 aqueous solution. Finally, Mn-AC was obtained by washing with abundant water and drying at 60 °C for 12 h.

For the MnO_2 positive electrode material, two aqueous solutions containing 0.15 g $KMnO_4$ and 0.2 g $MnSO_4•H_2O$ were mixed and stirred for 30 min. The precipitation separated by filtration was washed with abundant water five times and then dried in air at 60 °C overnight.

2.2 Characterization of samples

The CO_2 and N_2 adsorption/desorption isotherms were obtained at 273 and 77 K using automatic volumetric adsorption instruments (ASAP 2020 V3.04 H and ASAP 2460 2.02). The morphology and elemental contents were investigated by scanning electron microscopy (SEM, FEI Nova 400 Nano SEM) with X-ray energy disperse spectrum (EDS). The Mn content was determined via inductively coupled plasma-optical emission spectroscopy (ICP-OES) using IRIS Advantage ER/S (Thermo Elemental). The X-ray diffraction (XRD) patterns were collected by an X' pert Pro MPD diffractometer with Cu Ka radiation. Static contact angle measurements by placing a droplet of water or 1 mol L^{-1} Na_2SO_4 solution on the surface of the electrodes

consisting of one of the carbon samples and polyvinylidene difluoride (PVDF) with a weight ratio of 9:1.

2.3 Electrochemical measurements

Carbon electrodes were fabricated by pasting mixtures of one of the carbon samples, acetylene black and PVDF with a weight ratio of 8:1:1 on substrates. MnO_2 electrodes were prepared by the same procedure with a ratio of 7:2:1. The accurate weight of the electrodes was read by a high-precision balance (MS105DU, Mettler Toledo, d = 0.00001 g). For a three-electrode cell, the carbon or MnO_2 electrode was used as a working electrode, while a platinum foil and a saturated calomel electrode (SCE) were used as a counter and reference electrode, respectively, in 1 mol L^{-1} Na_2SO_4 electrolyte. Further, the Mn-AC and MnO_2 electrodes were assembled to construct asymmetrical supercapacitors. All cyclic voltammetry (CV) and galvanostatic charge discharge (GCD) measurements were performed by electrochemical workstation CHI660E and the cyclic performances were measured by a LAND CT2001A system.

3. Results and discussion

The commercial AC had a Brunauer-Emmett-Teller (BET) specific surface area (SSA) of 1944 m^2 g^{-1}, giving rise to a specific capacitance of 150 F g^{-1} in 6 mol L^{-1} KOH electrolyte (Fig. S1). However, only 94 F g^{-1} of specific capacitance was obtained when 1 mol L^{-1} Na_2SO_4 was used. In order to desire the high-energy asymmetrical supercapacitors, it was essential to study the capacitive behaviors of the different carbon samples based on the AC in the Na_2SO_4 electrolyte. The Zn-AC and Mn-AC could be

obtained by re-activation and oxidative etching of the AC with yields of 89.9% and 96.9%, respectively. The EDS analyses exhibited that the O contents of the AC and Zn-AC were 4.3 and 5.8 at% while that of the O content of the Mn-AC 8.0 at%. Moreover, the EDS of the Mn-AC showed no Mn element. The ICP-OES was further applied to check the content MnO_2 produced by reaction between C and $KMnO_4$[21] after washing with HCl/H_2O_2, revealing that the Mn weight content of Mn-AC is below 0.001%. The EDS and ICP-OES results illuminated that the O content obviously increased by oxidative etching method with $KMnO_4$ and finally MnO_2 was completely removed by HCl/H_2O_2.

The N_2 and CO_2 adsorption/desorption isotherms of the AC, Zn-AC and Mn-AC are shown in Fig. 1a and its inset. Obviously, all the samples exhibit type I adsorption desorption isotherms, confirming that the microporous structures dominated. The AC had the maximum BET SSA of 1944 $m^2\ g^{-1}$ and total pore volume of 1.08 $cm^3\ g^{-1}$. The SSAs of the Zn-AC and Mn-AC decreased to 1854 and 1329 $m^2\ g^{-1}$, respectively. Strictly, the BET method is not applicable to micropores, and hence the obtained BET SSA should be considered as an apparent area.[22] However, total pore volumes of Zn-AC and Mn-AC also declined to 1.05 and 0.71 $cm^3\ g^{-1}$, respectively. It was concluded that the oxidative etching decreased the SSA and pore volume more severely. Fig. 1b displays the results of pore distribution from CO_2 and N_2 adsorption by applying a non-local density functional theory (NLDFT) kernel, in which CO_2 adsorption giving the ultramicron pore distribution ranging from 0.45 to 0.93 nm while N_2 from 0.93 to 3.00 nm. The AC has multimodal pore distribution with the typical maxima at 0.84, 0.87 and

1.18 nm. After re-activation, pores at 0.84 nm for the AC disappear, instead, pores at 0.86 nm appear and the differential volume increases to the highest value of 2.05 cm^3 g^{-1} nm^{-1} of the three carbon samples, indicating that re-activation broaden the partial ultramicropores of the AC from 0.84 to 0.86 nm within which Zn^{2+} was absorbed. The Mn-AC has a different porous structure from the Zn-AC and AC, which shows a maximum at 0.89 nm with a lower differential volume of 1.02 cm^3 g^{-1} nm^{-1} and absence of pores at 0.87 nm for the AC, suggesting that $KMnO_4$ consumed C within and around the dominant micropores.

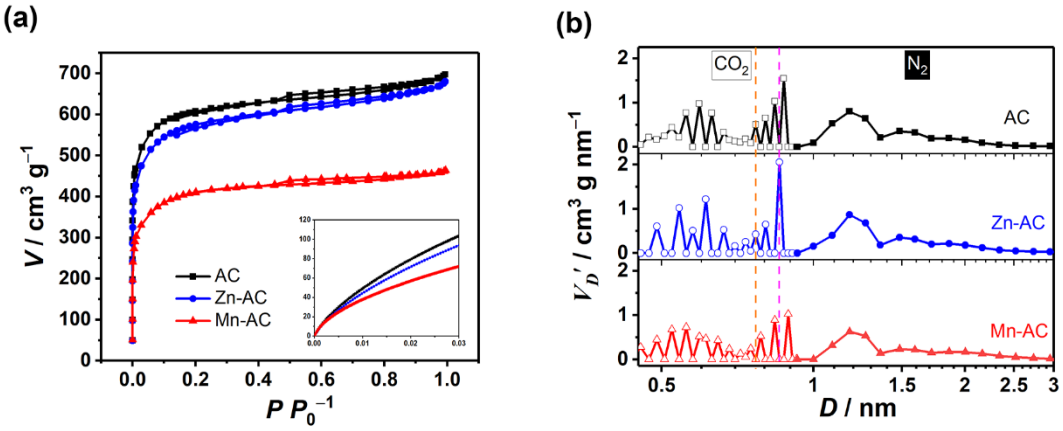

Fig. 1 (a) N_2 adsorption-desorption isotherms with CO_2 adsorption-desorption isotherms, and (b) pore distributions of AC, Zn-AC and Mn-AC.

In order to detect the electrolyte wettablity of the carbon materials, the Static contact angle was measured. It is found that the water contact angles of the AC, Zn-AC and Mn-AC are 121°, 125°, 101° and the Na_2SO_4 contact angles are 133°, 137°, 124°, respectively, as shown in Fig. S2 and S3. Overall, the wettability of the three carbon materials were comparable. It was also concluded that the changed pore distribution by re-activation slightly diminished the wettability for the Zn-AC and the increased O

content by oxidative etching slightly promoted the wettability for the Mn-AC, comparing with the original AC.

The electrochemical properties of the AC, Zn-AC and Mn-AC were estimated by CV and GCD measurements using three-electrode cells in the potential range from –1.0 to 0.6 V *vs*. SCE in the Na_2SO_4 electrolyte. Fig. 2a describes their cyclic voltammograms (CVs) at a scan rate of 10 mV s^{-1}, featuring quasi-rectangular shape without obvious redox peaks. Obviously, the AC exhibited the smallest area among all, suggesting that both the Zn-AC and Mn-AC had superior specific capacitances. Accordingly, Fig. 2b shows the GCD curves for the three samples. Considering that coulombic efficiency should not be beyond 100 %, the specific capacitances were calculated from the curves with shorter time.[23] Both the Zn-AC and Mn-AC had the same specific capacitance value of 132 F g^{-1} at 1 A g^{-1}, which was 40 % higher than 94 F g^{-1} for AC at the same specific current. On the other hand, the densities of the AC, Zn-AC and Mn-AC were calculated to be 0.66, 0.56 and 0.74 g cm^{-3} respectively according to the thickness (Fig. S4) and the weight of the electrode.[24] Therefore, the volumetric capacitances of the AC, Zn-AC and Mn-AC were determined to be 62, 74 and 98 F cm^{-3} respectively. The highest volumetric capacitance of the Mn-AC combining with its higher yield suggested that the oxidative etching method was more beneficial than the re-activation for practice application.

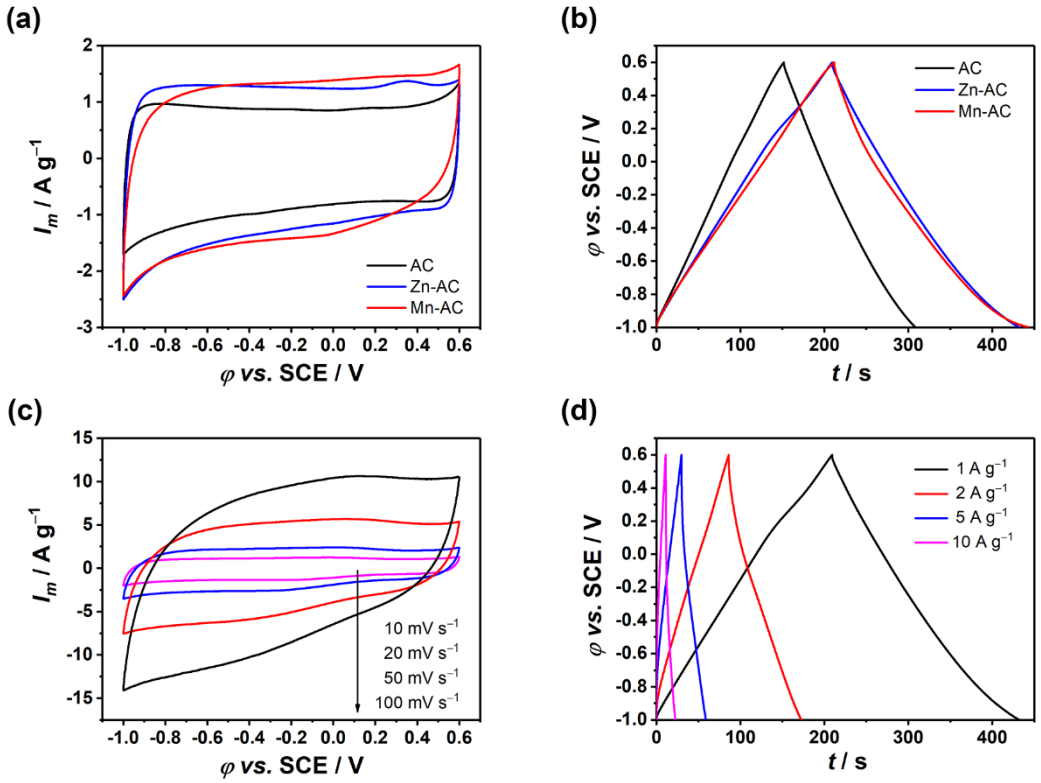

Fig. 2 Three-electrode electrochemical performances of carbons. (a) CVs at 10 mV s^{-1} and (b) GCD curves at 1 A g^{-1} of AC, Zn-AC and Mn-AC, (c) CVs at different scan rates from 10 to 100 mV s^{-1} and (d) GCD curves at different specific currents from 1 to 10 A g^{-1} of Mn-AC.

Different carbon materials based on the commerical AC with changed pore structure provided good objects to study the relationship between pore and ions of the Na_2SO_4 electrolyte. According to the literatures,[25, 26] the radii of hydrated Na^+ and SO_4^{2-} are 0.358 and 0.379 nm, respectively. In Fig. 1b, the orange dash line at 0.76 nm corresponds to the diameter of hydrated SO_4^{2-}. For re-activation, as mentioned above, the wettability of the Zn-AC was even slightly worse than the AC, which ruled out that the highly distorted solvated shell was merely squeezed into the ultramicropores in the Zn-AC rather than the AC. As the specific capacitance of the Zn-AC was evidently

higher than that of the AC, meant that the differential volume (sum) of the ion-accessible micropores of the Zn-AC were higher than that of the AC. According to the pore distributions, it is only possible that the micropores with the diameter beyond 0.85 nm can provide efficient SSA for hydrated Na^+ and SO_4^{2-} electrolyte ions, corresponding to the magenta dash line in Fig. 1b. Between 0.85 and 0.93 nm, the differential volume of the Zn-AC is 1.32 times as that of the AC, which is close to 1.40 times for specific capacitance. Therefore, the enhanced capacitive behavior of the Zn-AC was mainly attributed to the increased ion-accessible SSA arising from the more reconstructed efficient ultramicropores after re-activation. For oxidative etching, the contact angle of the Mn-AC was comparable to the orignal AC, especially for Na_2SO_4, while increased O content of the Mn-AC would certainly lead to lower conductivity, comparing with the AC. Hence, it could be ruled out that the highly distorted solvated shell was merely squeezed into the ultramicropores in the Mn-AC rather than the AC. Moreover, although the Mn-AC had the dominant ultramicropores with larger size of 0.89 nm, the corresponding differential volume is lower than that of AC. Thus, the enhanced capacitive behavior of the Mn-AC was mainly assigned to psudocapacitance arising from a larger oxygen content (8.0 %) in the Mn-AC comparing with 4.3 % for AC. The CV cathodic peak of the Mn-AC at −0.015 V in the Fig. 2a also indicates the existance of psudocapacitance. All in all, it was concluded that the threshold diameter of the ion-accessible micropores in the three carbon samples for hydrated Na^+ and SO_4^{2-} was 0.85 nm, meaning that that highly distorted solvated shell squeezed into the ultramicropores was ruled out.

Despite the same specific capacitances obtained by these two methods, oxidative etching had an obviously advantage of convenience and low cost, because the etching course occurred at room temperature, avoiding the high temperature re-activation. More importantly, due to its high yield and high volumetric capacitance, the Mn-AC was worth being further studied as the working electrode in three-electrode cells and negative electrodes in asymmetrical supercapacitors for pratice application. Fig. 2c shows the CVs of the Mn-AC at different scan rates from 10 to 100 mV s^{-1}, indicative of a stable potential window of 1.6 V in 1 mol L^{-1} Na_2SO_4. It is observed that the distortion of the rectangle occurs at the fast scan, which indicates the electrode resistance is larger, causing the smaller actual potential than applied externally potantial.[27] According to the GCD curves in Fig. 2d, the specific capacitances of the Mn-AC were calculated to be 132 F g^{-1} at 1 A g^{-1} and 94 F g^{-1} at 5 A g^{-1}, respectively.

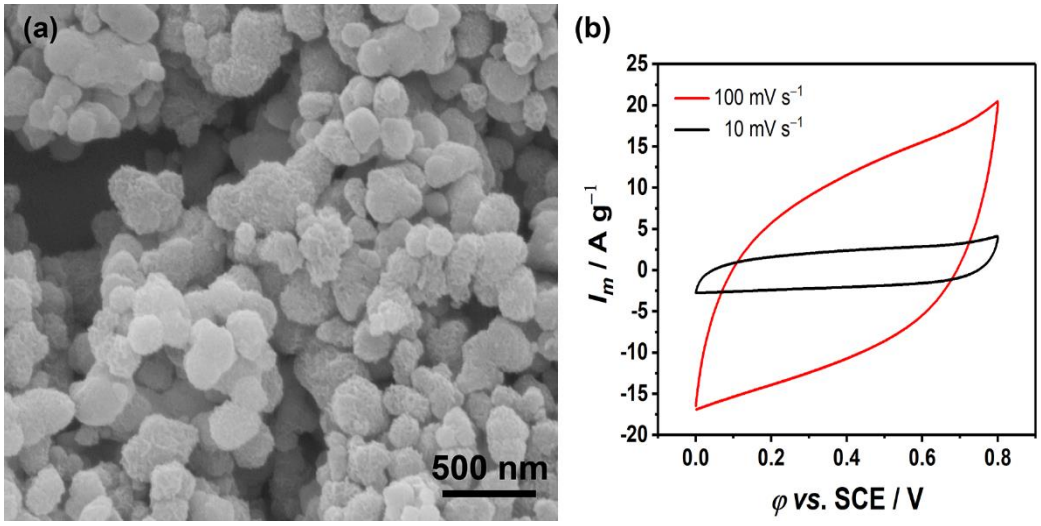

Fig. 3 (a) SEM image of MnO_2 and (b) CVs of MnO_2 in a three-electrode cell.

The positive electrode materials of the asymmetrical supercapacitors were prepared by a reaction between Mn^{2+} and Mn^{7+}. The XRD pattern of the positive

electrode material is shown in Fig. S5. The two broad peaks at 37° and 65.7° are indexed to ε–MnO_2 (JCPDS: 089-5171) with poor crystallinity. The EDS analysis revealed that the atomic ratio of Mn, O and K was 1 : 1.92 : 0.08, consisting with the stoichiometry of MnO_2. Fig. 3a shows the SEM images of MnO_2, which exhibits ball-like morphology with an average diameter of 200 nm. The rectangular CVs are obtained for the MnO_2 at the scan rates of 10 and 100 mV s^{-1} with the potential range from 0 to 0.8 V *vs*. SCE in the 1 mol L^{-1} Na_2SO_4 electrolyte (Fig. 3b), demonstrating that MnO_2 also had a good capacitive behavior. According to the GCD curves in Fig. S6, the specific capacitance of MnO_2 reaches 230 F g^{-1} at 1 A g^{-1}.

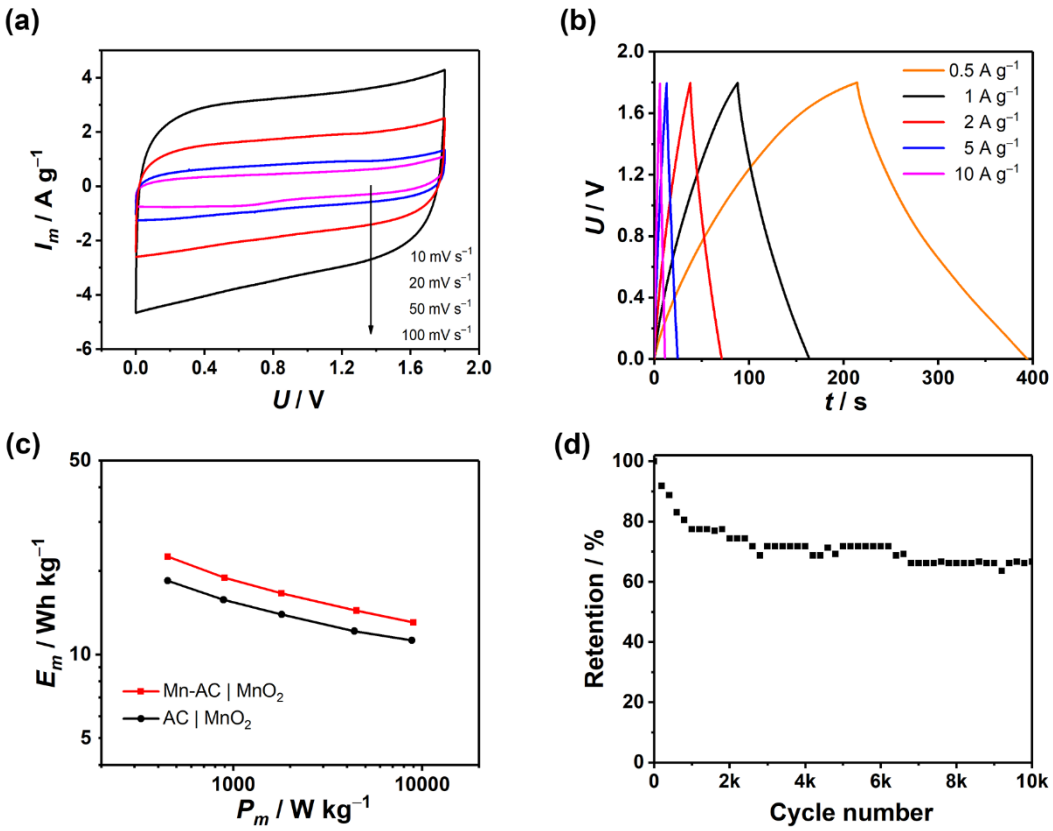

Fig. 4 (a) CVs and (b) GCD curves of asymmetrical Mn-AC | MnO_2 supercapacitor, (c) specific energies as a function of specific powers of Mn-AC | MnO_2 and AC | MnO_2 supercapacitors, (d) cyclic performance of Mn-AC | MnO_2 supercapacitor at 1 A g^{-1}.

In the three-electrode cells, the Mn-AC and MnO_2 electrodes could be measured within potential ranges of –1 to 0.6 V and 0 to 0.8 V *vs*. SCE at a scan rate of 10 mV s^{-1} (Fig. S7), respectively, suggesting that the asymmetrical (−) Mn-AC | 1 mol L^{-1} Na_2SO_4 | MnO_2 (+) (Mn-AC | MnO_2 in short) supercapacitors had 1.8 V of potential window. For asymmetrical cells, the amount of charge Q stored in each of the positive and negative electrodes must be the same, and is governed by the following Equation 1, where C_p and C_n are the capacitance, and U_p and U_p are the working potential range of the positive and negative electrodes in the cell.[28-30]

$$Q = C_p U_p = C_n U_n \quad (1)$$

The negative and positive working potential ranges were respectively from −1 to 0 V and 0 to 0.8 V *vs*. SCE, the voltage ratio U_n/U_p was determined to be 1.25. Thus, the optimal capacitance ratio C_p/C_n was also 1.25 in the asymmetrical supercapacitor. The asymmetrical two-electrode supercapacitors were constructed using the ε-MnO_2, Mn-AC and 1 mol L^{-1} Na_2SO_4 as positive and negative electrode and aqueous electrolytes. Fig. 4a and S8 show CVs of the asymmetrical supercapacitor with a voltage of 1.8 V at different scan rates. It was worth noting that the asymmetrical supercapacitor exhibited ideal capacitive behavior with a nearly rectangular shape even at a high scan rate of 500 mV s^{-1}. Fig. 4b shows the GCD curves of the asymmetrical Mn-AC | MnO_2 supercapacitor at different specific current densities. The specific capacitances of the asymmetrical supercapacitor were 50 F g^{-1} at 0.5 A g^{-1} and 29 F g^{-1} at 10 A g^{-1} according to the discharge curves, respectively. Therefore, the maximum specific energy for the

Mn-AC | MnO_2 supercapacitor was calculated to be 22.5 Wh kg^{-1} based on the total mass of active materials on the two electrodes, which was 22 % higher than 18.5 Wh kg^{-1} for the AC | MnO_2 supercapacitor. In addition, 9000 W kg^{-1} of the specific power was obtained when the Mn-AC | MnO_2 supercapacitor kept a reasonable specific energy of 13.1 Wh kg^{-1} while 8804 W kg^{-1} when the AC | MnO_2 supercapacitor 11.3 Wh kg^{-1} (Fig. 4c). The superior performance of the Mn-AC | MnO_2 supercapacitor was completely assigned to higher specific capacitance of Mn-AC. The cyclic performances of the asymmetrical cell are shown in Fig. 4d. 71.8 and 66.7 % of the initial capacitance could be retained at 1 A g^{-1} after 3000 and 10000 cycles, respectively. The capacitance fading may be mainly due to the potential polarization on the MnO_2 electrode.

4. Conclusions

In summary, the porous structure of the commercial AC has been changed by re-activation with $Zn(NO_3)_2$ and oxidative etching with $KMnO_4$, respectively. Re-activation broadened the partial ultramicropores of the AC by absorbing Zn^{2+} within them. Oxidative etching severely decreased the SSA and pore volume but increased the O content. The specific capacitances of the Zn-AC and Mn-AC were increased to 132 F g^{-1} from 94 F g^{-1} for the original AC. Combining the pore distribution with specific capacitances of the three carbon samples, it was inferred that the threshold diameter of the ion-accessible micropores in the three carbon samples for hydrated Na^+ and SO_4^{2-} was 0.85 nm, meaning that that highly distorted solvated shell squeezed into the ultramicropores was ruled out. The enhanced capacitive behaviors of the Zn-AC and

Mn-AC in 1 mol L^{-1} Na_2SO_4 were mainly attributed to the increased ion-accessible SSA and pseudocapacitance, respectively. For pratice applicaiton, the oxidative etching with $KMnO_4$ at room temperature was much more facile and economic approach to improve the specific capacitance of carbon. The asymmetrical Mn-AC | MnO_2 supercapacitors assembled in 1 mol L^{-1} Na_2SO_4 aqueous electrolyte had a high operating voltage of 1.8 V. A maximum specific capacitance of 50 F g^{-1} and specific energy of 22.5 Wh kg^{-1} was obtained at 0.5 A g^{-1}. Moreover, a high specific power of 9000 W kg^{-1} was achieved at 13.1 Wh kg^{-1}. Therefore, it is believed that either increasing the efficient micropores or the O content could improve the capacitive behavior of carbon in the Na_2SO_4 electrolyte. Oxidative etching method is also a general and low-cost method comparing with re-activation for carbon based supercapacitors.

Acknowledgement

This work was supported by State Key Laboratory of Materials Processing and Die & Mould Technology, Huazhong University of Science and Technology (P2019-014), National Natural Science Foundation of China (21905216), Natural Science Foundation of Hubei Province, China (2019CFB131) and Opening Project of Engineering Research Center of Nano-Geo Materials of Ministry of Education of China University of Geosciences (NGM2020KF005). The authors thank Asso. Prof. Liang Huang and Mr. Jun Zhang in Wuhan University of Science and Technology for the help of static contact angle measurements and Lei Peng and Zhiyue Tang for experiment

assistance in the revision.

References

1. Y. Chen, C. Yan and O. G. Schmidt, *Adv. Energy Mater.*, **3**, 1269 (2013).
2. L. Zou, Y. Jiang, J. Cheng, Y. Chen, B. Chi, J. Pu and L. Jian, *Electrochimica Acta*, **262**, 97 (2018).
3. G. Z. Chen, *Int. Mater. Rev.*, **62**, 173 (2017).
4. Y. Chen and G. Z. Chen, in *Innovations in engineered porous materials for energy generation and storage applications*, R. Rajagopalan and A. Balakrishnan Editors, p. 86, CRC press, Boca Raton (2018).
5. J. Xu, X. Wang, X. Zhou, N. Yuan, S. Ge and J. Ding, *Electrochimica Acta*, **301**, 478 (2019).
6. S. Tan and K. D. Li-Oakey, *J. Electrochem. Soc.*, **166**, A3294 (2019).
7. T. Liu, F. Zhang, Y. Song and Y. Li, *J. Mater. Chem. A*, **5**, 17705 (2017).
8. Y. Chen and G. Z. Chen, *Acta Phys.-Chim. Sin.*, **35**, 1904025 (2020).
9. T. Mitravinda, K. Nanaji, S. Anandan, A. Jyothirmayi, V. S. K. Chakravadhanula, C. S. Sharma and T. N. Rao, *J. Electrochem. Soc.*, **165**, A3369 (2018).
10. M. Zhang, S. Makino, D. Mochizuki and W. Sugimoto, *J. Power Sources*, **396**, 498 (2018).
11. M. Zhang, Y. Li and Z. Shen, *J. Power Sources*, **414**, 479 (2019).
12. X. Sun, X. Zhang, H. Zhang, D. Zhang and Y. Ma, *J. Solid State Electrochem.*, **16**, 2597 (2012).
13. P. Przygocki, Q. Abbas and F. Béguin, *Electrochimica Acta*, **269**, 640 (2018).
14. Q.-Z. Zhang, D. Zhang, Z.-C. Miao, X.-L. Zhang and S.-L. Chou, *Small*, **14**,

1702883 (2018).

15. S. Wu, K. S. Hui and K. N. Hui, *Carbon*, **132**, 776 (2018).
16. M. Vijayakumar, R. Santhosh, J. Adduru, T. N. Rao and M. Karthik, *Carbon*, **140**, 465 (2018).
17. N. Díez, R. Mysyk, W. Zhang, E. Goikolea and D. Carriazo, *J. Mater. Chem. A*, **5**, 14619 (2017).
18. J. Chmiola, G. Yushin, Y. Gogotsi, C. Portet, P. Simon and P. L. Taberna, *Science*, **313**, 1760 (2006).
19. D. G. Gromadskyi, J. H. Chae, S. A. Norman and G. Z. Chen, *Appl. Energy*, **159**, 39 (2015).
20. H. Sun, H. Gu, L. Zhang and Y. Chen, *Mater. Lett.*, **216**, 123 (2018).
21. X. Jin, W. Zhou, S. Zhang and G. Z. Chen, *Small*, **3**, 1513 (2007).
22. Y. Zhu, S. Murali, M. D. Stoller, K. J. Ganesh, W. Cai, P. J. Ferreira, A. Pirkle, R. M. Wallace, K. A. Cychosz, M. Thommes, D. Su, E. A. Stach and R. S. Ruoff, *Science*, **332**, 1537 (2011).
23. L. Zhang, H. Gu, H. Sun, F. Cao, Y. Chen and G. Z. Chen, *Carbon*, **132**, 573 (2018).
24. S. Lin, C. Zhang, Z. Wang, S. Dai and X. Jin, *Adv. Energy Mater.*, **7**, 1700766 (2017).
25. E. R. Nightingale, *J. Phys. Chem.*, **63**, 1381 (1959).
26. J. H. Chae and G. Z. Chen, *Electrochim. Acta*, **86**, 248 (2012).
27. J. H. Chae and G. Z. Chen, *Particuology*, **15**, 9 (2014).
28. C. Peng, S. Zhang, X. Zhou and G. Z. Chen, *Energy Environ. Sci.*, **3**, 1499 (2010).

29. Z. Dai, C. Peng, J. H. Chae, K. C. Ng and G. Z. Chen, *Sci. Rep.*, **5**, 9854 (2015).

30. S. G. Krishnan, M. Harilal, B. Pal, I. I. Misnon, C. Karuppiah, C.-C. Yang and R. Jose, *J. Electroanal. Chem.*, **805**, 126 (2017).

Supporting Information

Effects of pore widening versus oxygenation on capacitance of activated carbon in aqueous sodium sulfate electrolyte

Lixing Zhang,[1] Yuqin Chi,[1] Xiaolei Sun,[5] Huazhi Gu,[1] Haijun Zhang,[1] Zhen Li,[2] Yao Chen,[1,z] and George Zheng Chen[1,3,4]

[1] The State Key Laboratory of Refractories and Metallurgy, College of Materials and Metallurgy, Wuhan University of Science and Technology, Wuhan 430081, China.

[2] Engineering Research Center of Nano-Geo Materials of Ministry of Education, China University of Geosciences, Wuhan 430074, China

[3] Department of Chemical and Environmental Engineering, Faculty of Engineering, University of Nottingham, Nottingham NG2 7RD, UK.

[4] Department of Chemical and Environmental Engineering, Faculty of Science and Engineering, University of Nottingham Ningbo China, Ningbo 315100, China.

[5] School of Materials Science and Engineering & National Institute for Advanced Materials, Tianjin Key Lab for Rare Earth Materials and Applications, Centre for Rare Earth and Inorganic Functional Materials, Nankai University, Tianjin 300350, China

[z] Corresponding author. E-mail: y.chen@wust.edu.cn

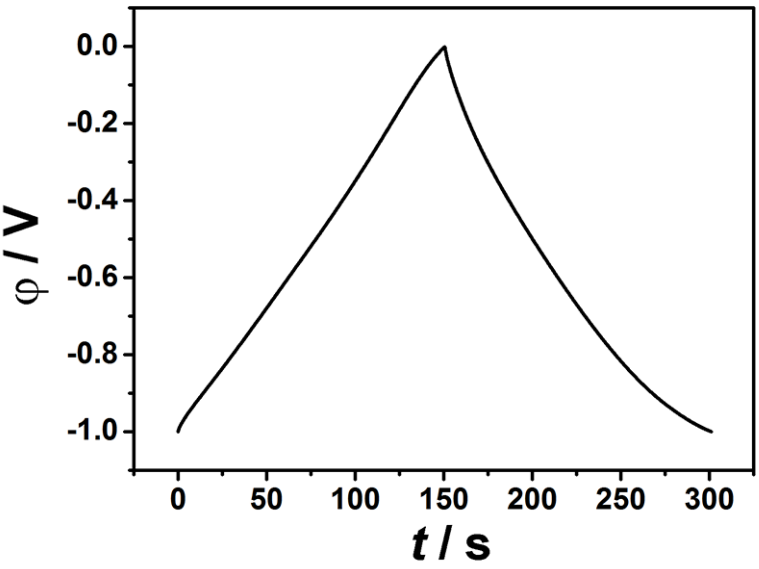

Fig. S1 GCD curve of AC at 1 A g^{-1} in 6 M KOH in a three-electrode cell.

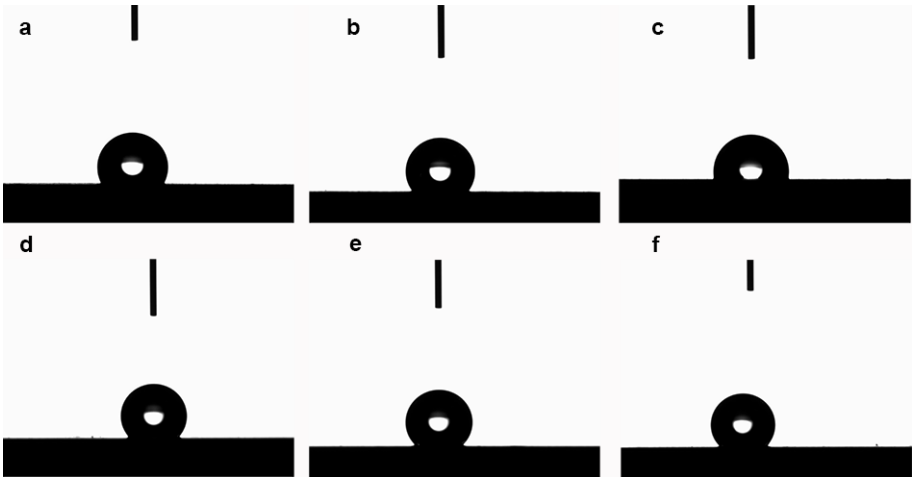

Fig. S2 Static water contact angles of (a) AC, (b) Zn-AC and (c) Mn-AC and Na_2SO_4 contact angles of (d) AC, (e) Zn-AC and (f) Mn-AC.

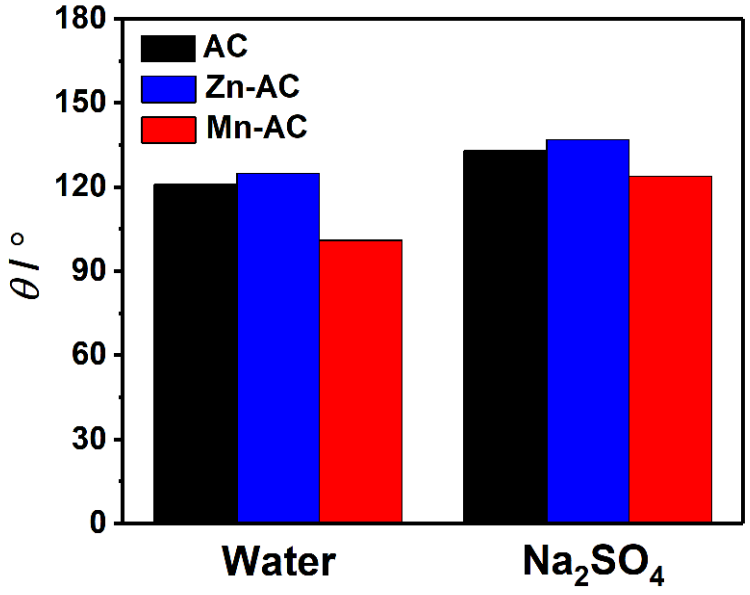

Fig. S3 Histogram of static water and Na_2SO_4 contact angles of AC, Zn-AC and Mn-AC.

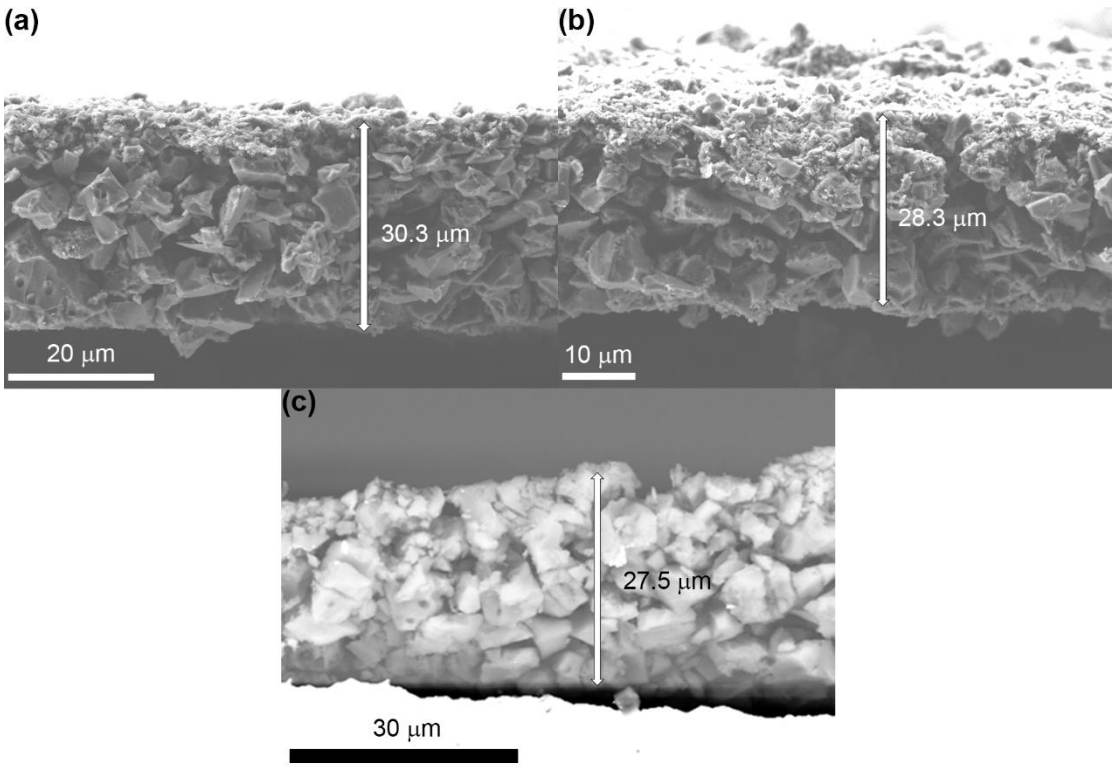

Fig. S4 Cross-section SEM images of (a) AC, (b) Zn-AC and (c) Mn-AC electrode.

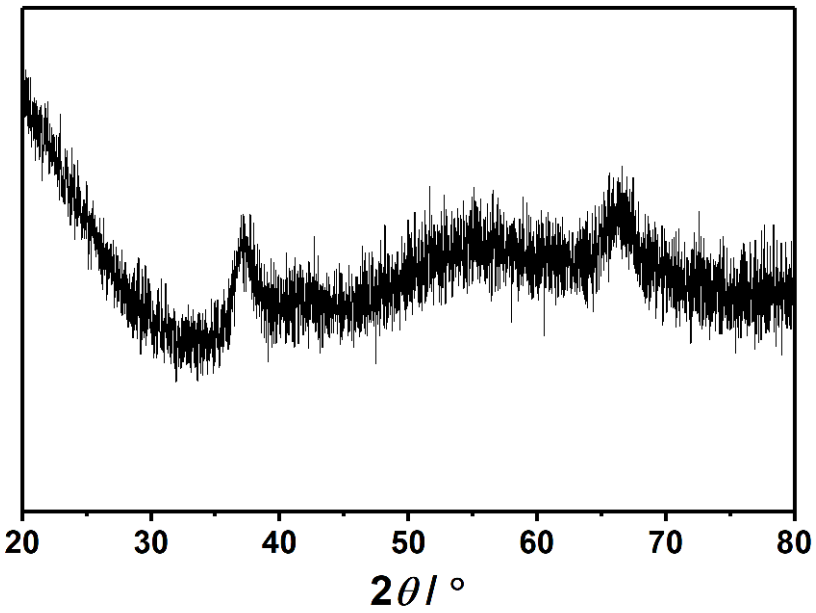

Fig. S5 XRD pattern of MnO_2.

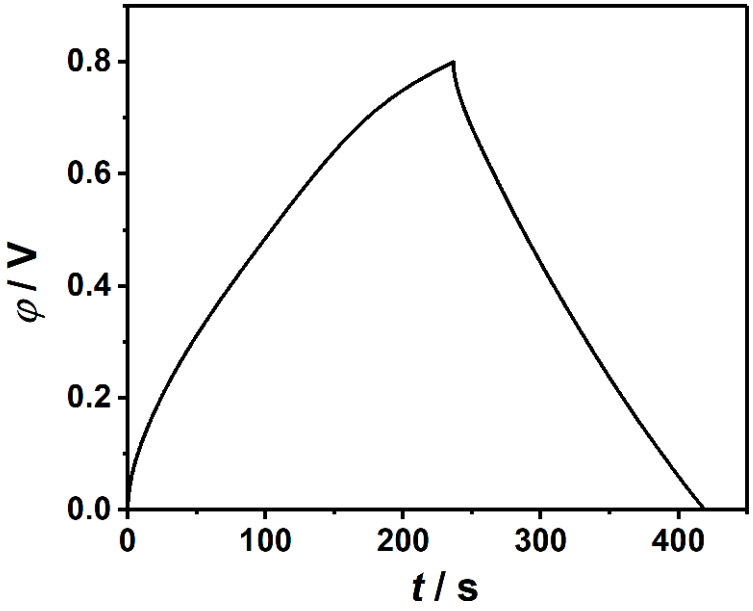

Fig. S6 GCD curve of MnO_2 at 1 A g^{-1}.

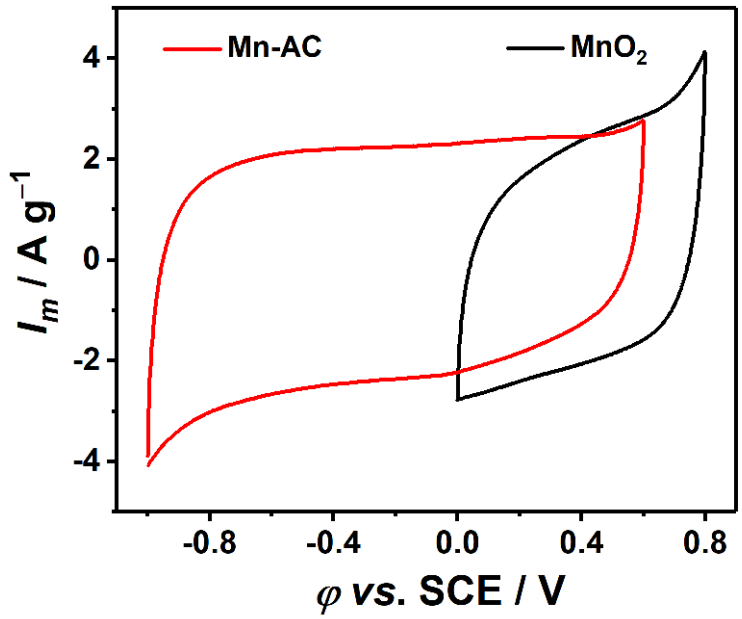

Fig. S7 CVs of Mn-AC and MnO_2 at 10 mV s^{-1}.

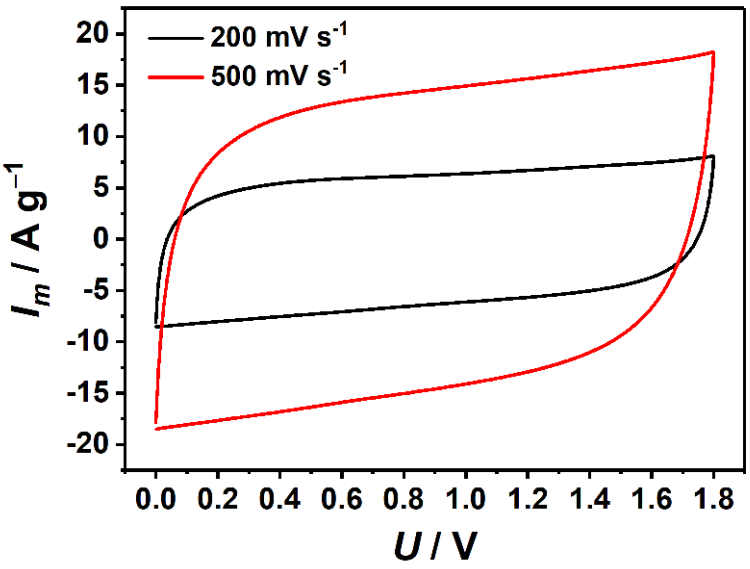

Fig. S8 CVs of Mn-AC | MnO_2 supercapacitor.